Monthly Notices
of the
ROYAL ASTRONOMICAL SOCIETY

MNRAS **496,** 1768–1783 (2020)
Advance Access publication 2020 June 06

doi:10.1093/mnras/staa1562

Comprehensive analysis of the transient X-ray pulsar MAXI J1409−619

Ç. K. Dönmez,[1] M. M. Serim,[1,2] S. Ç. İnam,[3★] Ş. Şahiner,[4] D. Serim[1] and A. Baykal[1★]

[1]*Physics Department, Middle East Technical University, 06800 Ankara, Turkey*
[2]*TÜBİTAK ULAKBİM, 06510 Ankara, Turkey*
[3]*Department of Electrical and Electronics Engineering, Başkent University, 06790 Ankara, Turkey*
[4]*Department of Electronics and Communication Engineering, Beykent University, 34398 İstanbul, Turkey*

Accepted 2020 June 2. Received 2020 May 31; in original form 2019 November 7

ABSTRACT

We probe the properties of the transient X-ray pulsar MAXI J1409−619 through *RXTE* and *Swift* follow-up observations of the outburst in 2010. We are able to phase-connect the pulse arrival times for the 25 d episode during the outburst. We suggest that either an orbital model (with $P_{\rm orb} \simeq 14.7(4)$ d) or a noise process due to random torque fluctuations (with $S_r \approx 1.3 \times 10^{-18}$ Hz^2 s^{-2} Hz^{-1}) is plausible to describe the residuals of the timing solution. The frequency derivatives indicate a positive torque–luminosity correlation, which implies temporary accretion disc formation during the outburst. We also discover several quasi-periodic oscillations in company with their harmonics whose centroid frequencies decrease as the source flux decays. The variation of the pulsed fraction and spectral power-law index of the source with X-ray flux is interpreted as the sign of transition from a critical to a sub-critical accretion regime at the critical luminosity within the range of 6×10^{37}–1.2×10^{38} erg s^{-1}. Using pulse-phase-resolved spectroscopy, we show that the phases with higher flux tend to have lower photon indices, indicating that the polar regions produce spectrally harder emission.

Key words: stars: neutron - pulsars: individual: MAXI J1409−619 - accretion – accretion discs.

1 INTRODUCTION

MAXI J1409−619 is a transient X-ray pulsar that was discovered by the Gas Slit Camera (GSC), one of the detectors of the *Monitor of All-sky X-ray Image* (*MAXI*) experiment, on 2010 October 17 with a (41 ± 7) mCrab peak flux in the 4–10 keV energy band (Yamaoka et al. 2010). Using Neil Gehrels Swift Observatory's (*Swift*) X-ray Telescope (XRT) observations, Kennea et al. (2010a) reported the source location as RA $14^{\rm h}08^{\rm m}02\overset{\rm s}{.}56$, Dec. $-61^\circ59'00\overset{''}{.}3$ in J2000 coordinates with an accuracy of 1.9 arcsec. The Two Micron All Sky Survey (2MASS) star 2MASS 14080271−6159020 was considered as the probable infrared (IR) counterpart of the source since it is 2.1 arcsec away from the source location (Kennea et al. 2010a). Orlandini et al. (2012) emphasized that no catalogued optical source is present at the source location (within an upper limit of 20 for the *R*-band magnitude) and suggested that this IR companion is a highly reddened late-O/early B-type star, implying the high-mass X-ray binary (HMXB) nature of the system. In addition, the closest source in the *Gaia* catalogue[1] is located 3.6 arcsec away from the reported X-ray position of the source (Kennea et al. 2010a) and hence it most likely does not represent the optical counterpart of the HMXB. On 2010 November 30, when MAXI J1409−619 underwent an outburst, becoming around seven times brighter compared to the initial observations, the *Swift* Burst Alert Telescope (BAT) was triggered to observe the source, revealing a 503 ± 10 s periodicity with 42 per cent pulsed fraction (Kennea et al. 2010b). Routine *MAXI*/GSC observations also indicated that the source was brightened significantly (Ueno et al. 2010). Utilizing the *Fermi* Gamma-ray Burst Monitor (GBM) observations on 2010 December 2–3, the source period was refined as 506.93(5) s, a frequency derivative of $1.66(14) \times 10^{-11}$ Hz s^{-1} was found, and the double-peaked nature of the pulse profile was revealed (Camero-Arranz, Finger & Jenke 2010). The spectra obtained from the *Rossi X-ray Timing Explorer* (*RXTE*)–Proportional Counter Array (PCA) observations on 2010 December 4 with a net exposure of 8.5 ks were modelled by a cut-off power law with either partially covered absorption or reflection of X-ray photons by cold electrons (see Magdziarz & Zdziarski 1995 for a detailed discussion about the reflection model) and a narrow iron line in both cases, with no sign of a cyclotron absorption feature (Yamamoto et al. 2010). In both models, the photon index was found to be $\Gamma \approx 1.3$ while a partially covered absorber $1.3 \pm 0.6 \times 10^{24}$ cm^{-2} is reported for the first

★ E-mail: inam@baskent.edu.tr (SÇİ); altan@astroa.physics.metu.edu.tr (AB)

[1]http://gaia.ari.uni-heidelberg.de/singlesource.html

© 2020 The Author(s)
Published by Oxford University Press on behalf of the Royal Astronomical Society

Downloaded from https://academic.oup.com/mnras/article/496/2/1768/5854204 by MIDDLE EAST TECHNICAL UNIVERSITY LIBRARY user on 17 August 2020

model or a reflection scaling factor of 0.52 ± 0.18 for the latter (Yamamoto et al. 2010). Orlandini et al. (2012) rediscovered the source from the archival *BeppoSAX* observations in 2000 at its low state. From these observations, the 1.8–100 keV energy spectrum was found to fit an absorbed power-law model with a photon index and hydrogen column density of $0.87^{+0.29}_{-0.19}$ and $(2.8^{+3.4}_{-2.2}) \times 10^{22}$ cm^{-2}. In addition to this spectral model, this broad-band spectrum revealed the presence of a cyclotron absorption feature with a fundamental energy of 44 keV leading to a magnetic field estimate of $3.8 \times 10^{12}(1 + z)$ G, where z is the gravitational redshift.

Kaur et al. (2010) announced the detection of a quasi-periodic oscillation (QPO) at 0.192 ± 0.006 Hz with two harmonics, using a total of 20 ks of observations on 2010 December 11. From archival observations of *BeppoSAX*, the *Advanced Satellite for Cosmology and Astrophysics* (*ASCA*), and the *INTErnational Gamma-Ray Astrophysics Laboratory* (*INTEGRAL*), it was inferred that MAXI J1409−619 was in a low state during the observations prior to its discovery (Sguera et al. 2010; Orlandini et al. 2012).

In this paper, we present the results of a comprehensive timing and spectral analysis of MAXI J1409−619, using the observations of *RXTE* and *Swift*. In Section 2, we give brief information about the observations and data reduction process. In Section 3, we present our timing and spectral analysis. In Section 4, we summarize and discuss our results.

2 OBSERVATIONS AND DATA REDUCTION

2.1 *RXTE*/PCA observations

RXTE, launched on 1995 December 30 and operational until 2012, was an observatory satellite dedicated to X-ray astronomy.[2] The PCA instrument onboard *RXTE* consisted of five identical proportional counter units (PCUs), each of which was sensitive to photon energies between 2 and 60 keV (Jahoda et al. 1996, 2006).

RXTE/PCA observations of MAXI J1409−619 took place between 2010 October 22 and 2011 February 5 (corresponding to the observation sets with proposal numbers 95358, 95441, 96410). A total of 50 observations is used in our analysis, amounting to a total exposure of 135.0 ks. Standard-2 mode data are used for extracting spectra (16 s timing resolution), and Good Xenon mode data are used for extracting light curves (∼1 μs timing resolution).

In order to process the *RXTE*/PCA data, good time intervals are selected. To apply background correction to spectra and light curves, Epoch 5C background models, being the latest models for the observations after 2004 provided by the *RXTE* Guest Observer Facility,[3] are used. Light-curve count rates are corrected to the total number of active PCUs and the Solar system barycentric correction is applied. As it was reported to be the most reliable PCU during our observations,[4] only PCU 2 data are used for spectral analysis, which leads to a total net exposure of 122.5 ks. The energy range used for the spectral analysis is 3–25 keV, and 0.5 per cent systematic error is applied to long and combined observations.

2.2 *Swift*/XRT observations

Swift is a multi-wavelength space observatory, launched on 2004 November 20. *Swift* is mainly used for gamma-ray burst monitoring, yet it has also proved its effectiveness in X-ray astronomy through an onboard 3.5 m focal length X-ray telescope (XRT) operating in the 0.2–10 keV energy range (Gehrels et al. 2004). Among a number of different operating modes of XRT, window timing (WT) mode has 1.8 ms high timing resolution but keeps only one-dimensional imaging data, whereas photon counting (PC) mode retains full spectroscopy and 600 × 602 pixel imaging information but with only 2.5 s timing resolution (Burrows et al. 2005)

32 *Swift*/XRT observations of MAXI J1409−619 were made between 2010 October 20 and 2011 January 28. Of these observations, 13 were conducted in PC mode, 17 in WT mode and 2 of them utilize both modes. Our analysis is based on the PC mode observations, each of which spans ∼1–2 ks, leading to a total exposure of 19.3 ks.

Data reduction is conducted using HEASOFT V6.22.1. Raw *Swift*/XRT data are reprocessed by the standard pipeline tool XRTPIPELINE V0.13.4 with default screening criteria. When the flux level of the source exceeds the pile-up limit (∼0.5 ct s^{-1}), pile-up corrections are performed. The source counts are gathered from a 20 pixel radius circle centred on the source while an inner circle of ∼5 pixel radius is excluded due to pile-up. Background emissions are estimated from source-free circular regions of 50 pixel radius. The first 30 channels of XRT data, corresponding to <0.3 keV, are marked 'bad' as XRT is not considered reliable below this energy range. The spectra are rebinned through GRPPHA in such a way that there are at least five counts per bin to obtain statistically significant spectra.

3 DATA ANALYSIS

3.1 Timing analysis

3.1.1 Pulse timing, timing solution and torque noise

In the timing analysis, we use a 0.125 s binned *RXTE*/PCA light curve that is extracted using the procedure described in Section 2. The 1 d binned light curve is shown in Fig. 1.

We search for the best frequencies by using statistically independent trial frequencies (Leahy, Elsner & Weisskopf 1983). Our search for the best frequencies is consistent with the pulse frequencies provided by the *Fermi*/GBM pulsar project team.[5] By folding the light curve at the pulse frequency, we construct pulse profiles with 20 phase bins for each observation. After performing χ^2 tests for all the constructed pulse profiles, the statistically strongest profile is assigned as the template pulse profile. Then, the pulse arrival times are computed by cross-correlating each individual pulse profile with the template. In the cross-correlation analysis, we use the harmonic representation of pulses (Deeter & Boynton 1985; see also İçdem, Baykal & Inam 2012 for applications).

We are able to phase-connect all pulse arrival times during the outburst. We fitted pulse arrival times to the cubic polynomial:

$$\delta\phi = \delta\phi_o + \delta\nu(t - t_o) + \frac{1}{2}\dot{\nu}(t - t_o)^2 + \frac{1}{6}\ddot{\nu}(t - t_o)^3 \quad (1)$$

where $\delta\phi$ is the pulse-phase offset, t_o is the epoch for folding; $\delta\phi_o$ is the residual phase offset at the time t_o; $\delta\nu$ is the correction to the

[2]The official cookbook for *RXTE* data analysis is located at https://heasarc.gsfc.nasa.gov/docs/xte/recipes/cook_book.html.
[3]https://heasarc.gsfc.nasa.gov/docs/xte/pca_bkg_epoch.html
[4]https://heasarc.gsfc.nasa.gov/docs/xte/recipes/pca_breakdown.html
[5]https://gammaray.nsstc.nasa.gov/gbm/science/pulsars.html

Downloaded from https://academic.oup.com/mnras/article/496/2/1768/5854204 by MIDDLE EAST TECHNICAL UNIVERSITY LIBRARY user on 17 August 2020

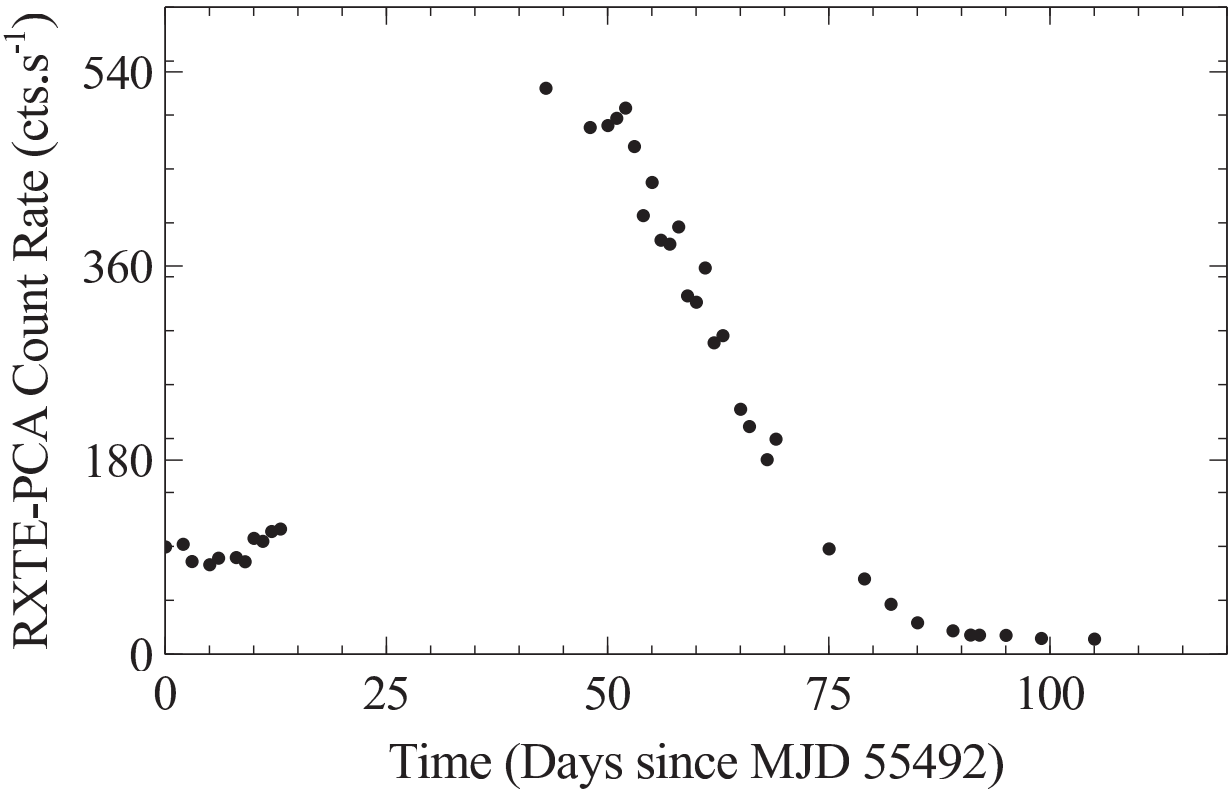


Figure 1. 2–60 keV 1 d binned *RXTE*/PCA light curve of MAXI J1409−619. Errors are smaller than the data points.

pulse frequency at t_0 with respect to the folded frequency ν_0; $\dot{\nu}$ and $\ddot{\nu}$ are the first and second time derivatives of pulse frequency.

The luminosity decreases almost linearly with time during the outburst as $L \sim L_0(- t/t_0)$. As the pulse frequency derivative exhibits a power-law dependence on luminosity in accretion disc models (e.g. Ghosh & Lamb 1979b; Torkelsson 1998; see also Section 3.1.2 for more detailed discussion on disc accretion) as $\dot{\nu} \propto L^{\gamma} \approx L_0^{\gamma}(-t/t_0)^{\gamma}$ where γ is the power-law index, the pulse frequency derivative is affected accordingly, implying a non-zero second time derivative $\ddot{\nu}$. Therefore a cubic polynomial fitting to the pulse arrival times describes pulse arrival times better than a quadratic fitting. In Fig. 2, we present the pulse phases and residuals of the pulse arrival times after the removal of a cubic polynomial.

The residuals after cubic polynomial fitting in Fig. 2 (middle panel) are consistent with a circular orbital model. In general, a model describing a circular orbit can be represented as:

$$\delta t_{\rm orb} = \frac{a_x \sin i}{c} \sin\left(\frac{2\pi(t - T_{\pi/2})}{P_{\rm orb}} + \frac{\pi}{2}\right) \quad (2)$$

where i is the inclination angle between the orbital angular momentum vector and the line of sight, $\frac{a_x \sin i}{c}$ is the light traveltime for projected semimajor axis, $T_{\pi/2}$ is the orbital epoch where the mean orbital longitude, $\frac{2\pi(t-T_{\pi/2})}{P_{\rm orb}} + \frac{\pi}{2}$, is maximum (i.e. 90°) and $P_{\rm orb}$ is the orbital period. The residuals are well fitted to the circular orbital model with a period of 14.7(4) d. The orbital model has decreased the reduced χ^2 from ∼35 to ∼1. The timing and possible orbital parameters obtained by the models are listed in Table 1. Using these orbital parameters, the mass function of the system results in

$$f(M) = \frac{4\pi^2 (a_x \sin i)^3}{G P_{\rm orb}^2} = \frac{(M_{\rm c} \sin i)^3}{(M_x + M_{\rm c})^2} \sim 0.1 {\rm M}_{\odot}, \quad (3)$$

where G is the gravitational constant, M_x is the mass of the neutron star and $M_{\rm c}$ is the mass of the companion star. A mass function of $\sim 0.1 {\rm M}_{\odot}$ indicates that MAXI J1409−619 should have a small inclination angle when we consider the probable O/early B-type companion (Orlandini et al. 2012). It should be noted that the data used for orbital modelling extend only to ∼25 d (see Fig. 2) and therefore future observations are required to ascertain the suggested orbital model above.

Then, every two consecutive pulse arrival times are fitted with a linear model since the slope of the linear models, $\delta\nu = \delta\phi/(t - t_0)$, enables us to compute the pulse frequencies corresponding to the mid-times of the fitted pulse arrival times. In Fig. 3, we present the pulse frequencies computed via this procedure together with the pulse frequencies measured through *Fermi*/GBM observations by the *Fermi*/GBM pulsar project team.

As an alternative to the aforementioned orbital model, the residuals of the cubic polynomial fit can also be interpreted as the noise process due to random torque fluctuations (Bildsten et al. 1997; Baykal et al. 2007). We estimate the noise strength by using the root mean square (rms) residuals of the cubic polynomial fit (Cordes 1980; Deeter 1984). In general, for the rth-order red noise (or the rth-order integral of white noise) with strength S_r, the mean square residual for data spanning an interval with length T is proportional to $S_r T^{2r-1}$. The expected mean square residual, after removing a polynomial of degree m over an interval of length T, is given by

$$< \sigma_R^2(m, T) >= S_r T^{2r-1} < \sigma_R^2(m, 1) >_u, \quad (4)$$

where $< \sigma_R^2(m, 1) >_u$ is the normalization constant for the unit time-scale, which can be estimated either by analytical evaluations or numerical simulations (Cordes 1980; Deeter 1984; Scott, Finger

Downloaded from https://academic.oup.com/mnras/article/496/2/1768/5854204 by MIDDLE EAST TECHNICAL UNIVERSITY LIBRARY user on 17 August 2020

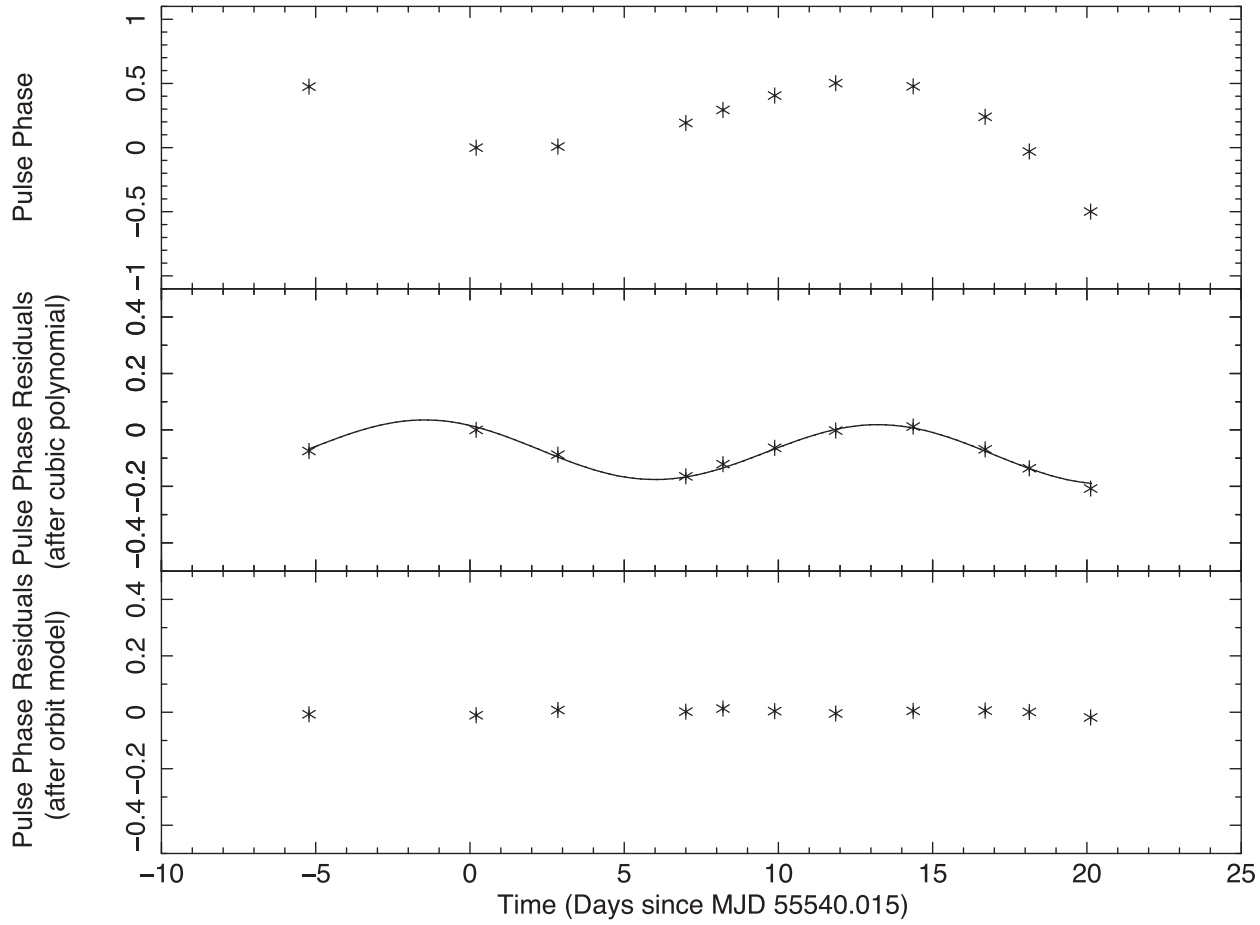


Figure 2. Upper panel: Pulse phases of MAXI J1409−619. Middle panel: Residuals of pulse phases after removal of a cubic polynomial. Lower panel: Residuals of pulse phases after removal of the orbit model. Errors are smaller than data marks.

Table 1. Timing solution of MAXI J1409−619. A number given in parentheses is the 1σ uncertainty in the least significant digit of a stated value.

Parameter	Value
Epoch (days in MJD)	55540.0150(6)
ν (10^{-3} Hz)	1.982 87(4)
$\dot{\nu}$ (10^{-11} Hz s^{-1})	1.599(9)
$\ddot{\nu}$ (10^{-18} Hz s^{-2})	− 6.4(8)
Orbital period (d)	14.7(4)
$a/c \sin i$ (s)	25.7(5)
Orbital epoch (days in MJD)	55547.5375(6)

& Wilson 2003). We use $m = 3$ for the cubic polynomial and $r = 2$ for second-order red noise in pulse arrival times (or pulse phases), which corresponds to first-order red noise in pulse frequency. We estimate the normalization constant by Monte Carlo simulation of observed time series for the second-order red noise process ($r = 2$) for a unit noise strength $S(r = 2)$. Our expected normalization constants are consistent with those obtained by direct mathematical evaluation (Cordes 1980; Deeter 1984). Using this technique, we found the noise strength associated with torque fluctuations for MAXI J1409−619 to be 1.3×10^{-18} Hz^2 s^{-2} Hz^{-1}, which is consistent with other accretion-powered pulsars (Baykal & Oegelman 1993; Bildsten et al. 1997).

3.1.2 Torque–luminosity correlations

Using *RXTE*/PCA observations between MJD 55531 and MJD 55575 corresponding to the high-luminosity region of the light curve, for which a temporary accretion disc formation is plausible, we investigate the relation between the torque and X-ray luminosity of the source using the pulse frequency derivative and count rate measurements conducted for each two-day long interval.

If the source accretes via an accretion disc, the standard accretion disc models (Ghosh & Lamb 1979b; Ghosh 1994; Torkelsson 1998; Kluźniak & Rappaport 2007) suggests a relation between the total external torque exerted on the neutron star and the bolometric luminosity of the source. For this case, the radius of the inner edge of the accretion disc (r_0) gets smaller as the accretion rate ($\dot{M}$) increases and can be approximated as (Pringle & Rees 1972; Ghosh & Lamb 1979a)

$$r_0 = K \mu^{4/7} (GM)^{-1/7} \dot{M}^{-2/7}, \tag{5}$$

where μ is the magnetic moment of the neutron star ($\mu \simeq BR^3$; B is the surface magnetic field and R is the radius of the neutron star), G is the universal gravitational constant, M is the mass of the neutron star, and K is a dimensionless parameter of the order of unity.

The total external torque estimate due to accretion can then be expressed as (Ghosh & Lamb 1979b)

$$2\pi I \dot{\nu} = n(\omega_s) \dot{M} l_K, \tag{6}$$

Downloaded from https://academic.oup.com/mnras/article/496/2/1768/5854204 by MIDDLE EAST TECHNICAL UNIVERSITY LIBRARY user on 17 August 2020

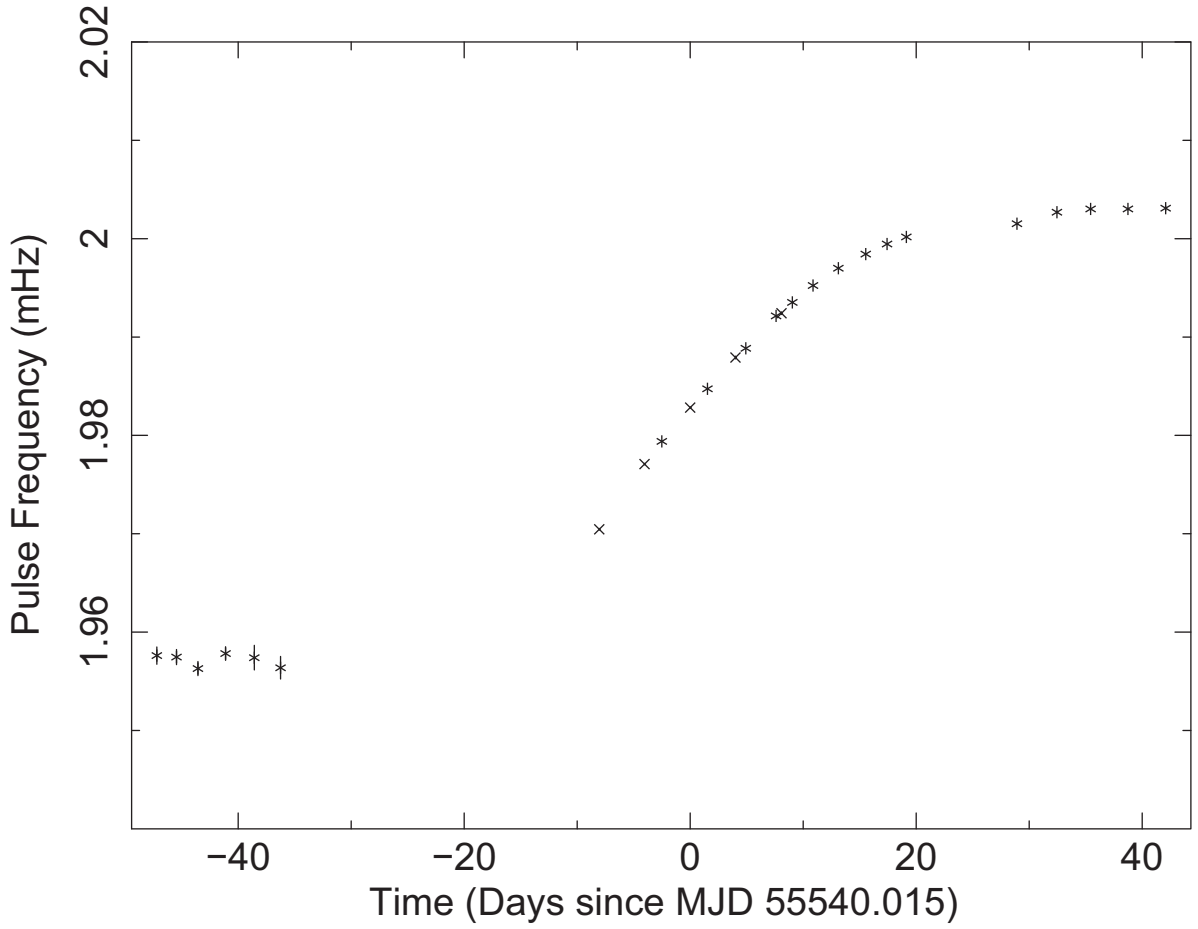


Figure 3. Pulse frequency measurements of MAXI J1409−619 deduced from pulse timing analysis of *RXTE*/PCA data (stars) together with the pulse frequencies measured by the *Fermi*/GBM pulsar project team (crosses).

where $l_K = (GMr_0)^{1/2}$ is the angular momentum per unit mass added by the disc to the neutron star at radius r_0 and I is the moment of inertia of the neutron star. In this equation, $n(\omega_s)$, called 'dimensionless torque', is approximately given by (Ghosh & Lamb 1979b; Klus et al. 2014)

$$n(\omega_s) \approx 1.4(1 - \omega_s/\omega_c)/(1 - \omega_s). \quad (7)$$

In the above equation, ω_s is the fastness parameter, which is equal to the ratio of the spin frequency of the neutron star to the Keplerian frequency at r_0 radius, which can be further expressed as

$$\omega_s = \nu/\nu_K(r_0) = 2\pi K^{3/2} P^{-1} (GM)^{-5/7} \mu^{6/7} \dot{M}^{-3/7}; \quad (8)$$

P is the spin period of the neutron star, $\nu_K(r_0)$ is the Keplerian angular frequency at r_0 and ω_c is the critical fastness parameter with a value of ∼0.35.

Due to the release of the gravitational potential energy of the accreted material, X-ray emission with a luminosity of

$$L = GM\dot{M}/R = \eta \dot{m} c^2 \quad (9)$$

occurs at the neutron star surface. In this equation, η is a dimensionless efficiency factor, which is about 0.1 for neutron stars. Using equations (5), (6) and (9), the relation between spin frequency derivative and X-ray luminosity can be written as

$$\dot{\nu} = \frac{n(\omega_s)}{2\pi I} K^{1/2} (GM)^{-3/7} \mu^{2/7} R^{6/7} L^{6/7}. \quad (10)$$

Equation (10) indicates a linear relationship between the frequency derivative and the sixth/seventh power of luminosity in the presence of strong material torques that give rise to a positive dimensionless torque close to unity. In Fig. 4, it is evident that the frequency derivative is directly proportional to the sixth/seventh power of the X-ray count rate with a slope of $(1.07 \pm 0.05) \times 10^{-13}$ (Hz s^{-1})(ct s^{-1})$^{-6/7}$, which is in accord with equation (10) with the assumption that the count rate from the 2–60 keV band is proportional to the bolometric X-ray luminosity. To relate equation (10) and Fig. 4, the 2–60 keV count rate of 350 ct s^{-1} is found to correspond to a luminosity of about 10^{38} erg s^{-1} for a distance of 15 kpc using WebPIMMS[6] using the absorbed power-law model with a photon index and hydrogen column density of $0.87^{+0.29}_{-0.19}$ and $(2.8^{+3.4}_{-2.2}) \times 10^{22}$ cm^{-2} respectively (Orlandini et al. 2012).

In equation (10), the proportionality constant is a function of $n(\omega_s)$ and B for given constant values of the neutron star mass $1.4M_\odot$, radius 10^6 cm, dimensionless parameters K unity, and moment of inertia 10^{45} g cm^2. Then, the value of B that minimizes the difference between the calculated slope and the measured slope $(1.07 \pm 0.05) \times 10^{-13}$ (Hz s^{-1})(ct s^{-1})$^{-6/7}$ is obtained by iteration (i.e. searching numerically for the B value) as $(2.67 \pm 0.44) \times 10^{11}$ G, yielding an $n(\omega_s)$ value of 1.397 ± 0.001. From equation (9),

[6]https://heasarc.gsfc.nasa.gov/cgi-bin/Tools/w3pimms/w3pimms.pl

Downloaded from https://academic.oup.com/mnras/article/496/2/1768/5854204 by MIDDLE EAST TECHNICAL UNIVERSITY LIBRARY user on 17 August 2020

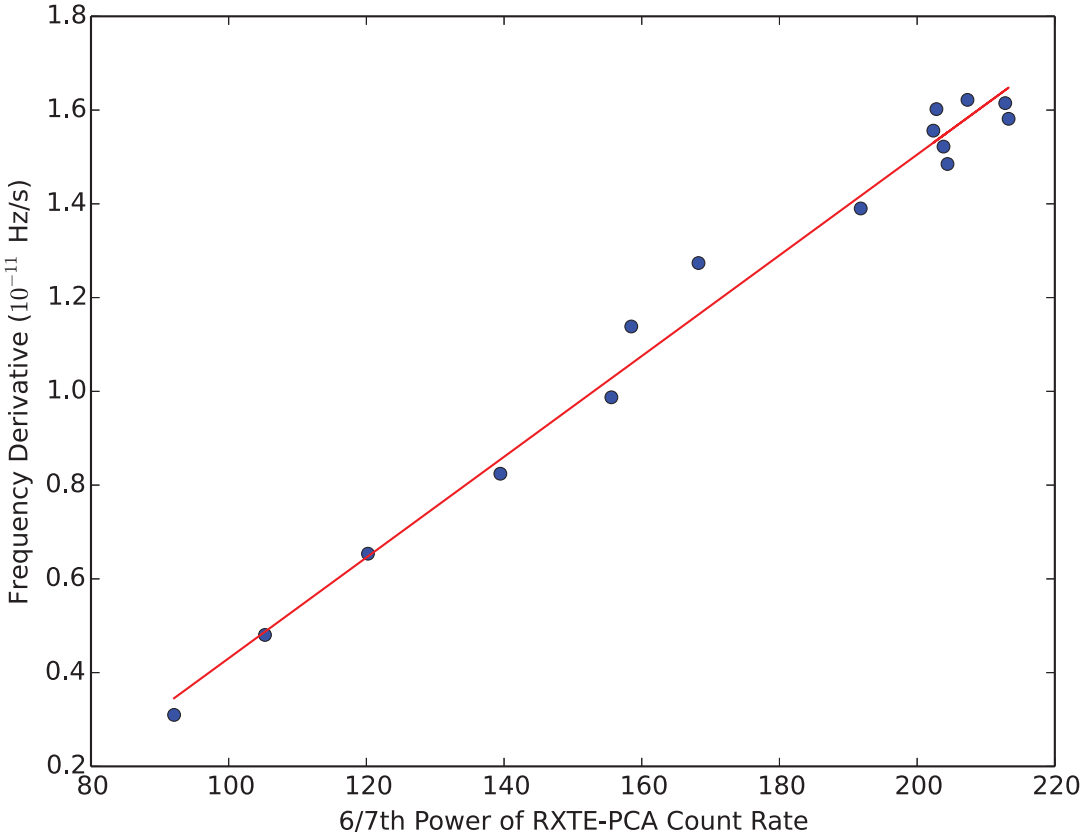


Figure 4. Measured frequency derivatives from *RXTE*/PCA observations as a function of the sixth/seventh power of the 2–60 keV *RXTE*/PCA count rate. The solid line indicates the best linear fit.

the mass accretion rate ($\dot{M}$) ranges from about 2.61×10^{17} g s^{-1} to about 7.41×10^{17} g s^{-1}. Using the obtained magnetic field value, the lower and upper values of $\dot{M}$ correspond to inner disc radius estimations (r_0) of about 1.21×10^8 cm and 0.90×10^8 cm respectively.

3.1.3 QPOs

To obtain power spectra from the *RXTE*/PCA light curve, the POWSPEC[7] tool is used. We generate the power spectra from short time segments and average them to increase the statistical significance of the spectra, since using long time-scales would increase the random scattering of the power estimates (van der Klis et al. 1987). The light curve is divided into 256 s long time intervals, each of which contains 1024 bins with 0.25 s rebinning time. Every consecutive nine intervals are averaged into one frame; therefore, each power spectrum plot spans 2304 s. Then, the results are rebinned by a factor of four. Analogous to other X-ray pulsars, the shape of a single power spectrum of the source can be defined by a broken power-law model. However, since many power spectra are combined into a single frame, variation in the break frequency with luminosity may smear out and smoothen the sharp transition between two power-law components (Mönkkönen et al. 2019 and references therein). Therefore, the continuum of the power spectra is represented by a smoothly broken power-law model, which is defined as

$$f(x) = A\left(\frac{x}{x_\mathrm{b}}\right)^{-\alpha_1}\left\{\frac{1}{2}\left[1+\left(\frac{x}{x_\mathrm{b}}\right)^{\frac{1}{\Delta}}\right]\right\}^{(\alpha_1-\alpha_2)\Delta} \tag{11}$$

where A is the amplitude, x is the frequency, x_b is the break frequency, α_1 and α_2 are the power-law indices at frequency $f < x_\mathrm{b}$ and $f > x_\mathrm{b}$, respectively, and Δ is the smoothness parameter.[8] The QPOs are identified as excess peaks in the continuum and are modelled as Lorentzian components added to the continuum model. The additive Lorentzian component is defined as

$$L = \frac{l_\mathrm{n}}{1+\left(2\times\frac{x-l_\mathrm{c}}{l_\mathrm{w}}\right)^2} \tag{12}$$

where x is the frequency, l_n is the line normalization parameter, l_c is the centre frequency of the line, and l_w is the line width (at full-width half-maximum). The harmonic peaks of QPO frequency that appear are also modelled with additional Lorentzian components. The fitting procedure is carried out using PYTHON libraries,[9] and we obtain the best parameters and their error ranges at the 1σ confidence level.

The significance of the QPO features is calculated by normalizing the power spectrum by dividing it by the modelled continuum and multiplying the result by two (van der Klis 1988). With the

[7] https://heasarc.gsfc.nasa.gov/lheasoft/ftools/fhelp/powspec.txt

[8] https://docs.astropy.org/en/stable/api/astropy.modeling.powerlaws.SmoothlyBrokenPowerLaw1D.html

[9] https://docs.scipy.org/doc/scipy/reference/generated/scipy.optimize.curve_fit.html

Downloaded from https://academic.oup.com/mnras/article/496/2/1768/5854204 by MIDDLE EAST TECHNICAL UNIVERSITY LIBRARY user on 17 August 2020

continuum normalized to two, a rebinning factor of four and the number of averaged intervals of nine, the resulting power spectrum continuum would be consistent with a χ^2 distribution for $2 \times 4 \times 9 = 72$ degrees of freedom (dof). As an example, a signal at an excess power of four (see Fig. 5, bottom panel) corresponds to a total power of $4 \times 4 \times 9 = 144$, and the probability of having a false signal, P, is calculated as $P(144|72) = 1.01 \times 10^{-6}$. We have 252 frequencies in each power spectra; therefore, the total probability of having a false signal is calculated as $252 \times 1.01 \times 10^{-6} = 2.53 \times 10^{-4}$, which corresponds to the 3.66σ level of detection (see İnam et al. 2004b; Acuner et al. 2014 for examples). We select the QPOs and their harmonics that have more than 3σ significance, as seen in Fig. 6. One example of a power spectrum fit and corresponding QPO and its harmonic are shown in Fig. 5. Furthermore, in order to indicate the coherence of oscillation signals (for QPOs), we also calculate the quality factors (Q values) of the corresponding Lorentzian components, simply defined as the ratio of the line width to the centroid frequency, which are also given in Table 2. The calculated quality factors are well above the broad-band noise level ($Q > 2$, see e.g. Acuner et al. 2014) and indicate clear detection of QPO signals.

QPOs are detected only during the first half of the decaying part of the outburst in 2010 December, and the signal possesses a transient nature, occasionally disappearing altogether in the power spectra. QPO harmonics seem to appear for most cases in which the principal Lorentzian component is observed, found around double the centroid frequency of the main QPO features, though many of these harmonics are not statistically significant.

Another notable result is that the QPO centroid frequencies decrease consistently over time. The first QPOs are detected around 0.2 Hz; however, as the outburst flux decays, QPO centroid frequencies decrease down to 0.1 Hz (see Fig. 6). As the source flux consistently decreases over the time period in which the QPOs are detected, we can conclude that QPO centroid frequencies are correlated with flux, similar to the case of A0535+262 (Finger, Wilson & Harmon 1996).

3.1.4 Pulsed fractions

Using the *RXTE*/PCA light curve, we calculate the pulsed fraction (P.F.) of the source for each observation. For our calculations, we use 20 binned pulse profiles and use the definition P.F. $= (I_{\rm max} - I_{\rm min})/(I_{\rm max} + I_{\rm min})$, where $I_{\rm min}$ and $I_{\rm max}$ are the count rates of the bins with the minimum and maximum count rates respectively. To demonstrate the flux dependence of the pulsed fraction of the source, we plot these measurements as a function of the *RXTE*/PCA count rate of the source in Fig. 7. The pulsed fraction exhibits a positive correlation with the count rate up to $\sim$200 ct s^{-1} (corresponding to a luminosity of $\sim 6 \times 10^{37}$ erg s^{-1} for the source distance suggested by Orlandini et al. 2012), beyond which the correlation switches to negative.

3.2 Spectral analysis

3.2.1 Time-resolved spectra

For *RXTE*/PCA spectral analysis, we first combine and fit all observations in the 95441 set (between MJD 55491 and 55597 with a total exposure of 74.4 ks) resulting in a single spectrum. While fitting, the 3–25 keV band is used, a systematic error of 0.5 per cent is set, and chi-statistics is utilized. An absorbed power-law model with a high-energy cut-off plus a Gaussian iron line fixed at 6.4 keV (PHABS∗(CUTOFFPL+GAUSS)) is employed to describe the resulting spectrum (see Fig. 8). The error ranges of the model parameters are calculated at the 90 per cent confidence level. For the PHABS component, the default solar abundances and photoionization cross-sections predefined in XSPEC are used (see Anders & Grevesse 1989; Verner et al. 1996 for the values).

Afterwards, the observations are fitted separately in order to investigate the evolution of the fit parameters over time. Subsequent short observations are combined before fitting when the exposure times are insufficient, leading to 37 statistically significant spectra. Following the same steps as in the analysis of the combined spectrum of the 95441 set, the spectra are generated within the 3–25 keV energy band. While modelling, the error range of parameters is calculated at the 90 per cent confidence level and the represented flux values are calculated in the 3–25 keV energy band. Most of the spectra are fitted with a model including the high-energy cut-off. However, as the count rates of the observations decrease, a decreasing signal-to-noise ratio causes the spectral quality to deteriorate, which prevents the fit converging, and therefore constrains the cut-off energy values. Therefore some spectra are fitted with a power-law model without the cut-off model. Additionally, a 0.5 per cent systematic error is set while fitting spectra of combined or long-duration observations. The evolution of the spectral parameters with time is presented in Fig. 9.

In general, the models accurately fit the spectra: only two spectra have reduced χ^2 values exceeding 2. The photon index values exhibit an inverse proportional relation with flux up to a certain degree, after which photon index values stay relatively flat. This relation is shown in Fig. 10. High-energy cut-off values are only obtained around the peak of the outburst and are decreasing over time. When MAXI J1409–619 was discovered in 2010 October, and at the tail of the outburst, the cut-off energies are not constrained and the spectra can be equivalently described without the cut-off component. In order to show the unconstrained nature of the cut-off component before the outburst peak, two contour plots before (MJD 55492) and during the outburst peak (MJD 55453) are plotted as in Fig. 11. Therefore it should be noted that within these time intervals, the photon indices are obtained without the cut-off model since the cut-off values are generally unconstrained at low flux observations.

Especially in long observations, a bump around 10 keV is evident in the residuals of the fits. This feature was mentioned by Coburn et al. (2002) and it has also been observed in many accreting X-ray pulsars (e.g. Her X−1 and 4U 1907+09), not only in *RXTE* data but also in *Ginga* and *BeppoSAX* data. Being always at around 10 keV, the feature is not considered to be a cyclotron line; therefore, it was concluded that it might be an intrinsic feature common in accreting pulsars. Even though its origin is not yet clear, this feature is attributed to the broadening of the cyclotron line due to Comptonization along the column (Farinelli et al. 2016).

Swift/XRT has a moderate spectral resolution, and no single observation of it has an exposure of more than 2 ks; therefore, observations close in time and having similar count rates are combined into six groups in order to increase the statistical significance of the resulting spectra. Additionally, considering the low count rates in the *Swift*/XRT observations, we proceed with the spectral analysis using C statistics (Cash 1979) via the CSTAT tool within XSPEC. The spectra are fitted simply with an absorbed power-law (PHABS∗POWERLAW) model. The errors of the model parameters are calculated at the 90 per cent confidence level, and the 0.5–10 keV flux of the entire model is derived via the CFLUX component. The given spectral model successfully fits the spectra, yet the spectral quality is inferior compared to the *RXTE*/PCA data (see Figs 12

Downloaded from https://academic.oup.com/mnras/article/496/2/1768/5854204 by MIDDLE EAST TECHNICAL UNIVERSITY LIBRARY user on 17 August 2020

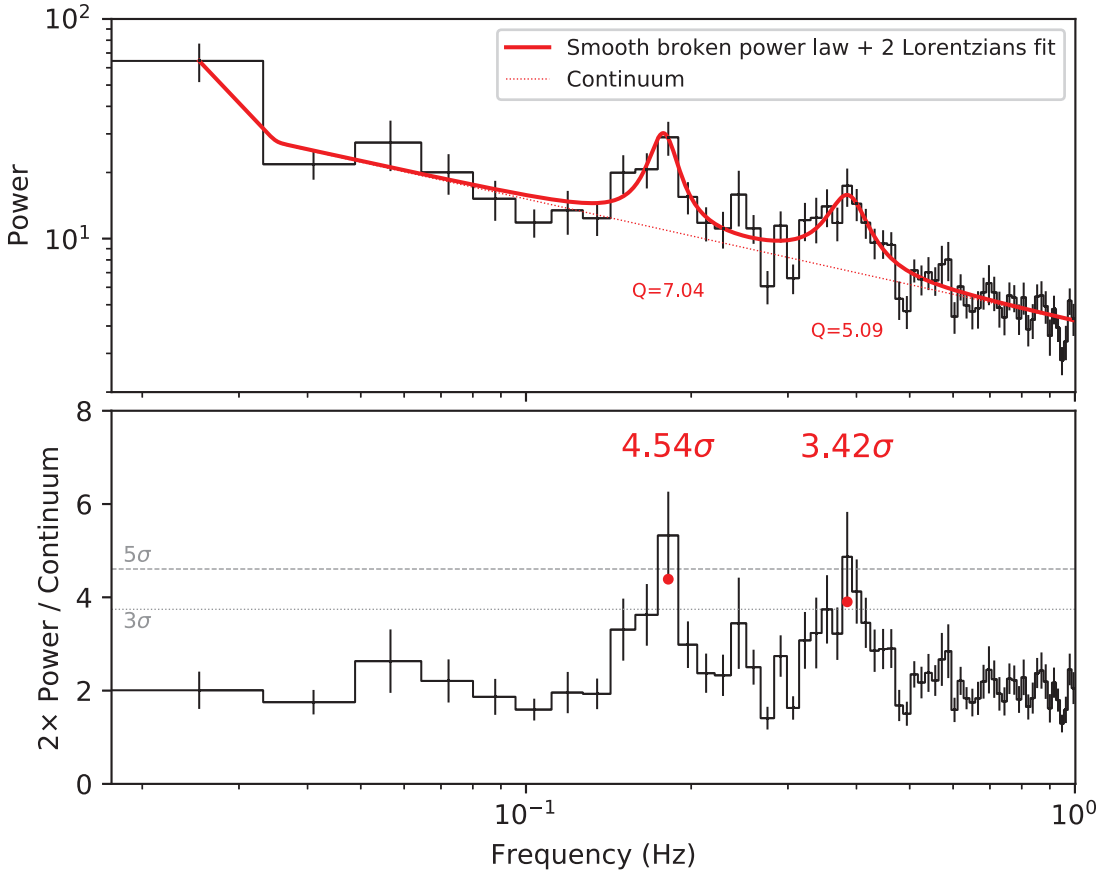


Figure 5. Upper panel: The power spectrum of the first 2304 s long segment of observation 95441-01-01-06 (MJD 55545). The dashed red line indicates the fit for the continuum and the solid red line represents the fit after the addition of Lorentzian components. Q values of the Lorentzian components are shown as well. Lower panel: The power spectra after normalization to the continuum and the detection levels of the excess signals (see the text below). The dashed lines indicate the 3σ and 5σ detection levels for the possible QPO structures.

(*Swift*/XRT) and 8 (*RXTE*/PCA) as an example for comparison). The evolution of the parameters is consistent with those obtained using the analysis of *RXTE*/PCA data. The reduced χ^2 values of the fits are between 0.72 and 1.21. The results of the spectral fitting of the *Swift*/XRT observations are given in Table 3.

3.2.2 *Pulse-phase-resolved spectra*

We perform pulse-phase-resolved spectral analysis for the three observations conducted by *RXTE*/PCA on 2010 December 11–12 (MJD 55541–55542) during the peak of the outburst, totalling a 34.0 ks exposure. A spin period of 503.62 s (1.9856 mHz) is used, which is found from timing analysis (see Section 3.1.1). A total of 10 phase bins is used; as a result, the spectrum of each phase bin is obtained from about 3.4 ks of exposure. The phase-resolved spectra are fitted by an absorbed power law with a high-energy cut-off plus a Gaussian iron line fixed at 6.4 keV. The reduced χ^2 values of the phase-resolved spectra range between 0.941 and 1.895. The pulse-phase dependence of the spectral parameters is presented in Fig. 13. The double-peaked nature of the pulse profile is evident in phase-dependent flux measurements. The neutral hydrogen column density $n_{\rm H}$ does not have a significant variation with changing phase. The photon index appears to be low during the pulse peaks, and the emission softens notably when the flux is minimum.

3.2.3 *Energy-dependent pulse profiles*

In addition to the pulse profile shown in the uppermost panel of Fig. 13, the energy dependence of pulse profiles is investigated as well. For this analysis, we use the same three *RXTE*/PCA observations that are also used for the pulse-phase-resolved spectral analysis (see Section 3.2.2). These observations, conducted on MJD 55541–55542, have flux levels around 1.6×10^{-9} erg cm^{-2} s^{-1}. The observations are combined, and the resulting data are folded using the previously found spin period of 503.62 s (see Section 3.1.1). Then, normalized phase profiles with 10 phase bins are created separately for the 3–8, 8–13, 13–18, 18–25, and 25–60 keV energy ranges using the FBSSUM tool.

As can be seen in Fig. 14, the pulse profiles of MAXI J1409−619 do not exhibit strong energy dependence; however, the pulsed fraction changes in different bands. While it is most prominent in the 8–13 keV energy band, it diminishes at higher energies, almost vanishing above 25 keV.

4 SUMMARY AND DISCUSSION

Using *RXTE*/PCA and *Swift*/XRT observations of MAXI J1409−619, we perform a timing and X-ray spectral analysis with the aim of constituting a more comprehensive perspective on the nature of this transient source.

Downloaded from https://academic.oup.com/mnras/article/496/2/1768/5854204 by MIDDLE EAST TECHNICAL UNIVERSITY LIBRARY user on 17 August 2020

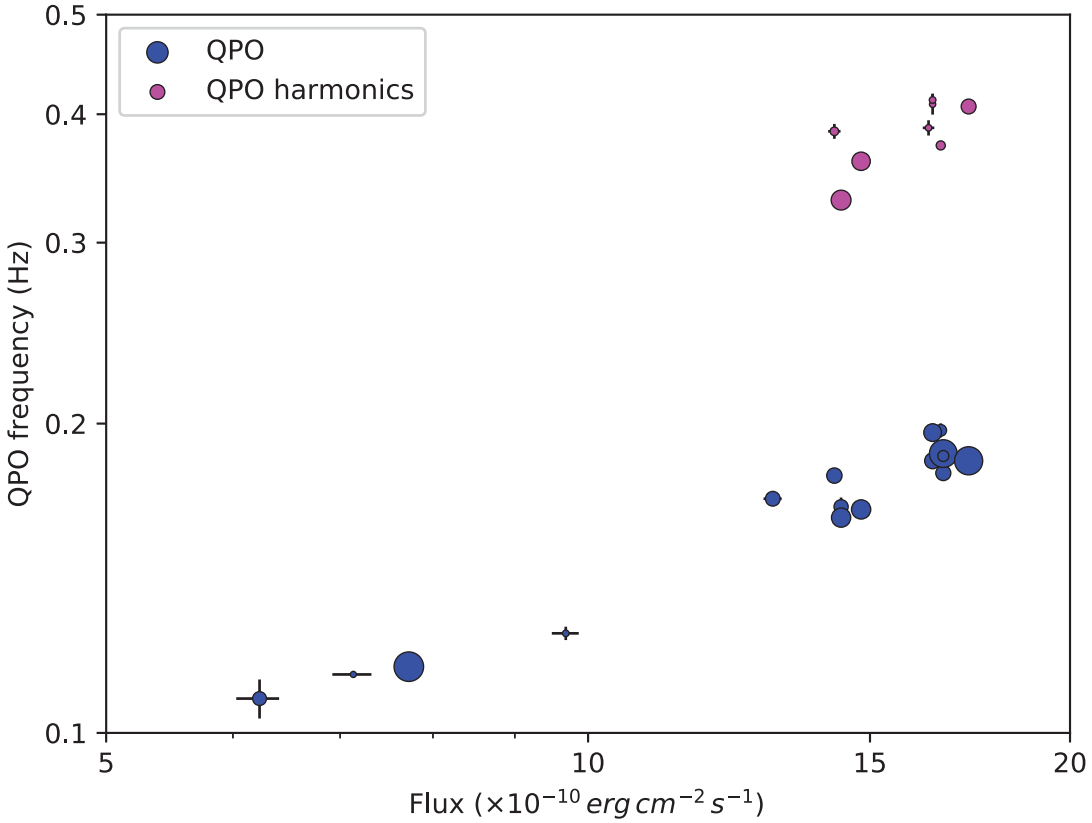


Figure 6. QPO centroid frequencies (blue circles) and QPO harmonics (magenta circles) versus flux. QPOs with only more than 3σ significance are included. The magnitude of the circular marks implies the significance level of the QPOs, and the biggest circle in the plot corresponds to 6.90σ. Errors smaller than the corresponding circles are not visible in the figure (see Table 2 for the QPO centroid frequencies).

Table 2. Detected QPOs of MAXI J1409−619.

Obs. ID	Epoch	ν_{QPO} (Hz)		Q value		Significance (σ)	
	(MJD)	#1	#2	#1	#2	#1	#2
95441-01-01-02	55541.621	0.197 ± 0.003	–	6.340	–	3.934	–
	55541.648	0.189 ± 0.002	0.373 ± 0.003	6.751	18.672	3.103	3.510
95441-01-01-00	55541.804	0.196 ± 0.003	0.409 ± 0.009	7.788	4.311	4.934	3.044
	55541.831	–	0.413 ± 0.006	–	20.630	–	3.103
	55541.957	0.184 ± 0.002	–	8.924	–	4.636	–
95441-01-01-03	55542.665	0.179 ± 0.003	–	3.620	–	4.491	–
	55542.709	0.187 ± 0.001	–	8.862	–	6.590	–
	55542.785	0.186 ± 0.002	–	4.279	–	3.822	–
95441-01-01-04	55543.818	0.184 ± 0.001	–	7.895	–	6.667	–
	55543.845	–	0.407 ± 0.003	–	19.310	–	4.467
95441-01-01-05	55544.798	–	0.388 ± 0.007	–	4.580	–	3.087
95441-01-01-06	55545.638	0.178 ± 0.002	0.385 ± 0.006	7.036	5.089	4.543	3.421
95441-01-01-07	55546.835	0.165 ± 0.003	0.360 ± 0.002	3.042	11.423	5.191	5.045
95441-01-02-00	55547.097	0.166 ± 0.003	0.330 ± 0.005	2.430	4.644	4.348	5.291
	55547.124	0.162 ± 0.002	–	6.661	–	5.186	–
95441-01-02-03	55549.395	0.169 ± 0.002	–	5.096	–	4.439	–
95441-01-03-00	55554.353	0.125 ± 0.002	–	5.388	–	3.089	–
95441-01-03-02	55556.705	0.116 ± 0.001	–	4.930	–	6.897	–
95441-01-03-03	55558.142	0.114 ± 0.001	–	5.253	–	3.003	–
95441-01-03-04	55559.644	0.108 ± 0.005	–	5.036	–	4.294	–

Downloaded from https://academic.oup.com/mnras/article/496/2/1768/5854204 by MIDDLE EAST TECHNICAL UNIVERSITY LIBRARY user on 17 August 2020

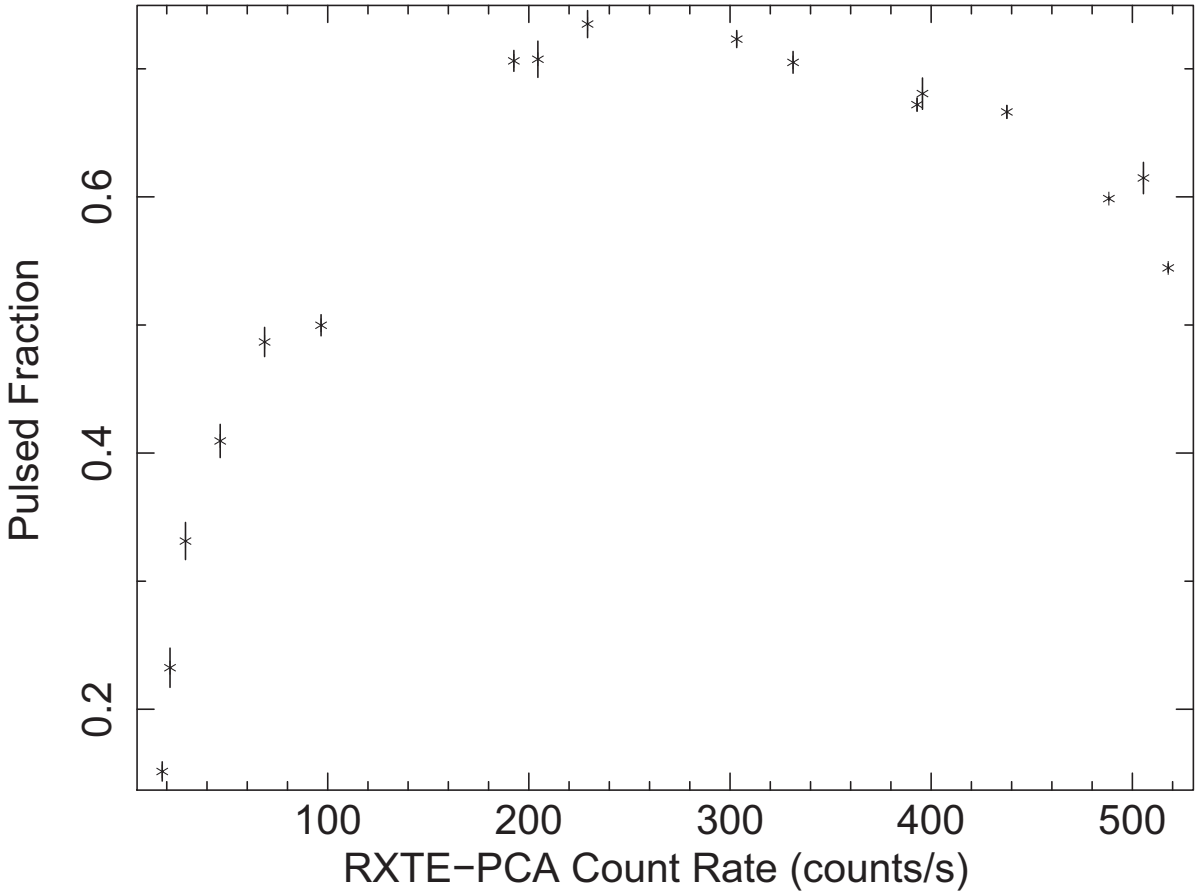


Figure 7. Pulsed fraction as a function of the 2–60 keV *RXTE*/PCA count rate of the source.

After fitting pulse arrival times to a cubic polynomial, we find that the residuals indicate a possible circular orbit with an orbital period of 14.7(4) d. This orbital model indicates a mass function of about $0.1 M_{\odot}$, implying that the orbital inclination angle should be very small. We also provide an alternative interpretation of these residuals as the noise process due to random torque fluctuations, which leads to a torque noise strength estimate of 1.3×10^{-18} Hz^2 s^{-2} Hz^{-1}, which is of the same order as some wind-accreting pulsars in HMXB systems and some disc-accreting pulsars in LMXB systems.

Torque fluctuations and the noise of accretion-powered pulsars have been studied for several sources (Baykal & Oegelman 1993; Bildsten et al. 1997). The noise strength associated with torque fluctuations is obtained for MAXI J1409−619 as 1.3×10^{-18} Hz^2 s^{-2} Hz^{-1}. This value of the noise strength estimate is of the same order as those of other accretion-powered sources such as wind accretors, e.g. Vela X−1, 4U 1538−52 and GX 301−2 with the values changing between 10^{-20} and 10^{-18} Hz^2 s^{-2} Hz^{-1} (Bildsten et al. 1997). Her X−1 and 4U 1626−67, which are disc accretors with low-mass companions, have shown pulse frequency derivatives consistent with noise strengths 10^{-21}–10^{-18} Hz^2 s^{-2} Hz^{-1} (Bildsten et al. 1997). Hence, the residuals of the cubic polynomial fit are also consistent with the torque noise fluctuation observed in other accreting sources.

We consider the correlation between pulse frequency derivative and X-ray count rate (see Fig. 4) as a consequence of disc accretion. Using standard accretion disc theory and assuming the distance to the source as 15 kpc, we estimate the surface dipole magnetic field strength as $(2.67 \pm 0.44) \times 10^{11}$ G corresponding to a range of inner disc radius values varying between about 0.90×10^8 and 1.21×10^8 cm. Our magnetic field strength estimate is about one order of magnitude smaller than the previous estimate of $\simeq 3.8 \times 10^{12}(1 + z)$ G obtained from cyclotron resonance spectral features (Orlandini et al. 2012). Our magnetic field estimate would be consistent with the estimate of Orlandini et al. (2012), if the distance to the source were to be taken as 9.5 kpc. In this case, the inner radius of the accretion disc should also change, ranging between about 5.60×10^8 and 7.53×10^8 cm.

QPOs with a very wide range of peak frequencies from 0.01–0.4 Hz have been observed in many accretion-powered pulsars (see İnam et al. 2004b; Acuner et al. 2014 and references therein). MAXI J1409−619 was the first neutron star observed to have harmonics of its QPO feature (Dugair et al. 2013). Afterwards, similar behaviour was also observed in 4U 0115+63, making MAXI J1409−619 and 4U 0115+63 the only two accreting X-ray pulsars known to show QPO harmonics (Roy et al. 2019).

QPOs have usually been interpreted either as the Keplerian frequency at the inner radius of the accretion disc (van der Klis et al. 1987) or the beat frequency of the Keplerian frequency at the inner radius of the accretion disc and the spin period of the neutron star (Lamb et al. 1985).

As seen from Fig. 6, centroid frequencies of detected QPOs decrease from 0.2 Hz to 0.1 Hz consistently with decreasing X-ray count rate while the outburst flux decays. Since these frequencies are much greater than the spin frequency of the source, we can solely interpret them to be equal to the Keplerian frequencies at the

Downloaded from https://academic.oup.com/mnras/article/496/2/1768/5854204 by MIDDLE EAST TECHNICAL UNIVERSITY LIBRARY user on 17 August 2020

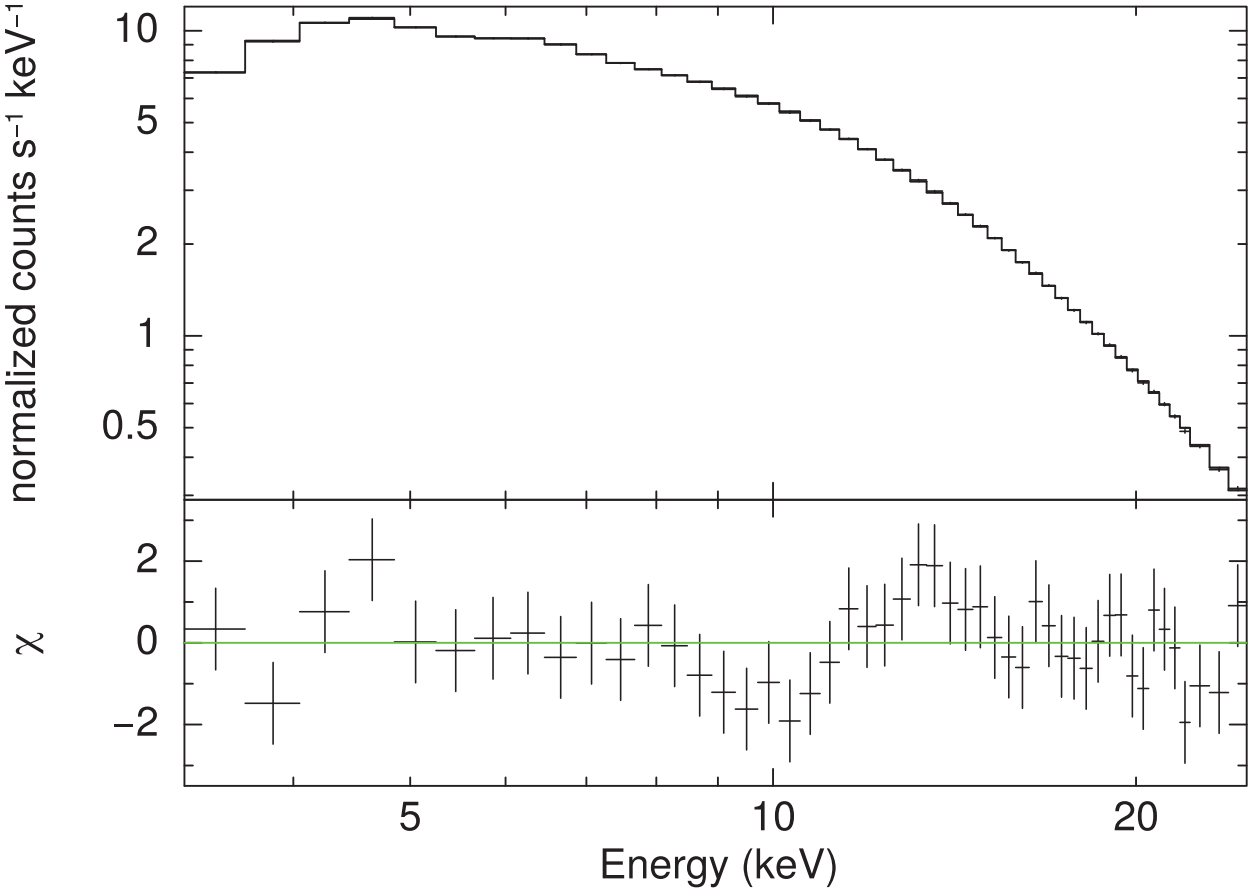


Figure 8. Upper panel: *RXTE*/PCA spectrum of the whole 95441 set (MJD 55540–55560, 74.4 ks) with a power-law fit with a high-energy cut-off plus a Gaussian iron line fixed at 6.4 keV. The reduced χ^2 of the fit is 1.014. The errors in the spectrum are too small to be visible. Lower panel: Residuals of the fit in σ values.

inner radius of the accretion disc while the inner disc varies with decreasing X-ray flux and then the inner disc radius can be related to the QPO centroid frequency ($\nu_{\rm QPO}$) as

$$r_0 = \left[\frac{(GM)^{1/2}}{2\pi\,\nu_{\rm QPO}}\right]^{2/3}. \quad (13)$$

From equation (13), our QPO frequencies indicate that the inner radius of the accretion disc moved outward from $r_0 = 4.9 \times 10^8$ cm to $r_0 = 7.8 \times 10^8$ cm as the outburst faded. It is important to note that this radius range almost coincides with the radius range (from 5.60×10^8 to 7.53×10^8 cm) obtained using standard accretion disc theory if the distance is taken as 9.5 kpc.

In Fig. 10, the spectral fits obtained from the lowest X-ray flux values ($<2 \times 10^{-10}$ erg s^{-1} cm^{-2}, corresponding to a 3–25 keV luminosity of about 5×10^{36} erg s^{-1} or a 2–60 keV luminosity of about 2.4×10^{37} erg s^{-1}) have significantly high power-law indices and are modelled by an absorbed power-law model without a high-energy cut-off component. On the other hand, for the measurements plotted as circles in Fig. 10, which are obtained using an absorbed power law with high-energy cut-off model, the power-law index has a weak trend of anticorrelation with X-ray flux up to $\sim 10^{-9}$ erg s^{-1} cm^{-2}, beyond which it is weakly correlated with X-ray flux. This flux level corresponds to a 3–25 keV luminosity of about 2.5×10^{37} erg s^{-1} or a 2–60 keV luminosity of about 1.2×10^{38} erg s^{-1}. This transition level from anticorrelation to correlation can be interpreted as the critical luminosity for which the accretion regime shifts from critical (high-luminosity) to sub-critical (low-luminosity) states. During the transition, the critical luminosity level can be approximately expressed as $\sim 1.49 \times 10^{37} (B/10^{12}G)^{16/15}$ erg s^{-1} for a neutron star of mass 1.4 $M_\odot$ and radius 10^6 cm (Becker et al. 2012). Using this relation regarding critical luminosity, the upper limit for magnetic field strength can be estimated as $\sim 7 \times 10^{12}$ G for a critical luminosity of $\sim 1.2 \times 10^{38}$ erg s^{-1} (see below for further discussion on the range of critical luminosity), which is closer to the value inferred from cyclotron resonance features by Orlandini et al. (2012); however, this value is 26 times greater than the value of magnetic field strength deduced from the torque model described in Section 3.1.2. This discrepancy could be understood (or resolved) in terms of the torque model in the following way: Since the angular acceleration is proportional to both magnetic moment and accretion luminosity $\dot{\nu} \sim \mu^{2/7} L^{6/7}$, the disagreement of the magnetic field values can be compensated if the luminosity is about $\sim$ 34 per cent of its original value corresponding to a distance of about 8.7 kpc.

Analogous to the behaviour of MAXI J1409–619, transition from anticorrelation to correlation between the photon index and the X-ray luminosity is observed in EXO 2030+375 (Epili et al. 2017). Positive and negative correlations with power-law index are also seen in sources with cyclotron features (Klochkov et al. 2011; Malacaria et al. 2015). For MAXI J1409–619, it should be noted that

Downloaded from https://academic.oup.com/mnras/article/496/2/1768/5854204 by MIDDLE EAST TECHNICAL UNIVERSITY LIBRARY user on 17 August 2020

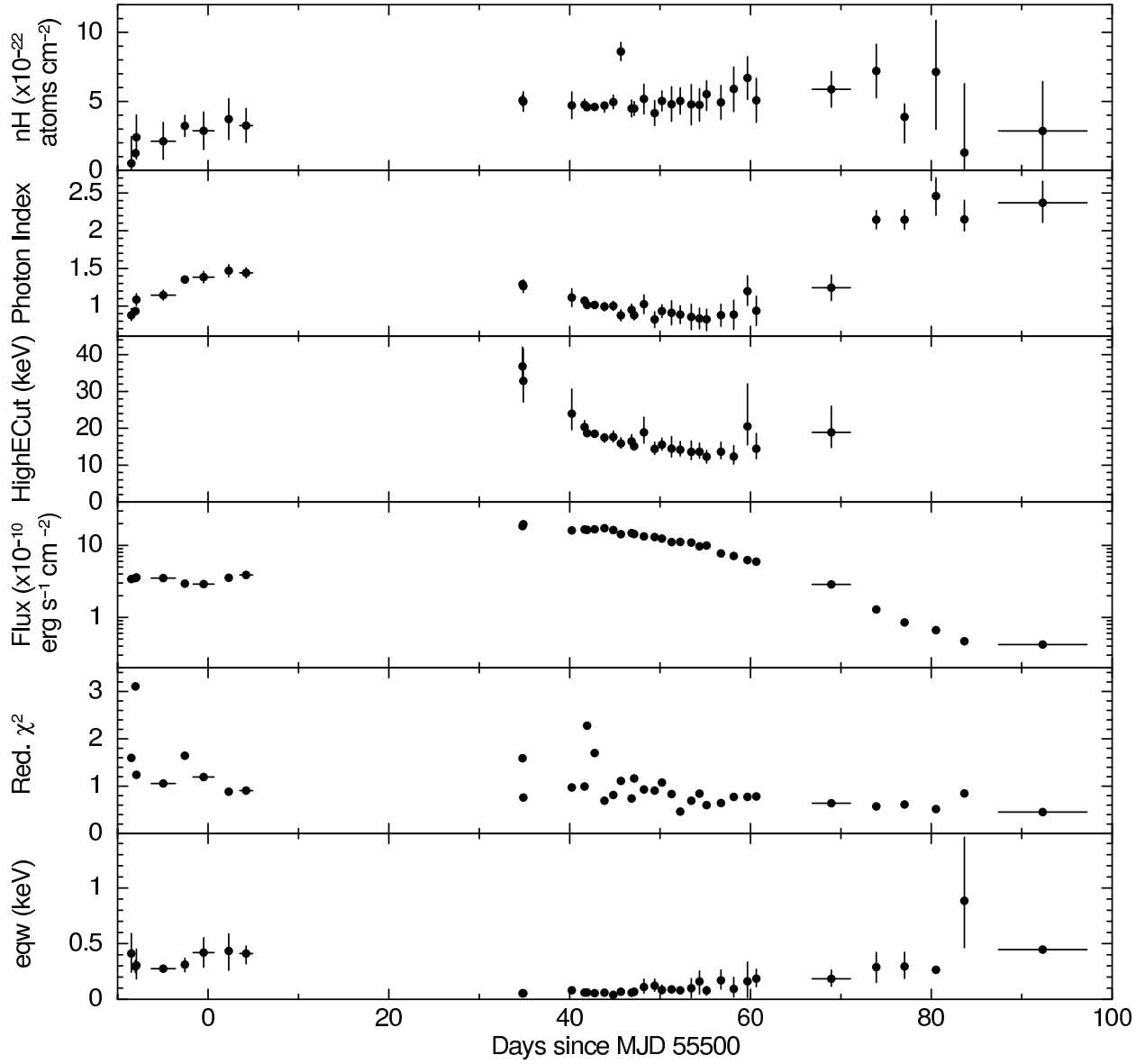


Figure 9. From top to bottom, the panels show the time evolution of the hydrogen column density ($n_{\rm H}$), photon index, cut-off energy, flux at 3–25 keV energy band, reduced χ^2 and equivalent width of the Gaussian component of *RXTE*/PCA observations. The error bars in flux are not seen as they are smaller than the data marks.

the starting flux level of positive correlation of spectral index may represent the upper limit of critical luminosity of the source, since the spectral index values are scattered and obtained via diferent spectral models at lower flux values.[10]

On the other hand, it is important to note that the pulse fraction of the source is correlated with the *RXTE*/PCA count rate up to 200 ct s^{-1} (see Fig. 7), corresponding to a 2–60 keV luminosity of about $\sim 6 \times 10^{37}$ erg s^{-1} if a distance of 15 kpc is assumed. Beyond this luminosity level, the pulsed fraction anticorrelates with the count rate. The observed anticorrelation can be interpreted as an increase of the unpulsed component of the emission of the pulsar in the form of a fan beam, as suggested by Becker et al. (2012) (see also Mushtukov et al. 2015). A similar kind of mode switching of correlation around critical luminosity is also observed in 2S 1417–624; at a lower flux level İnam et al. (2004a) reported a positive correlation of pulse fraction and flux, while Gupta, Naik & Jaisawal (2019) reported a negative correlation for the same source when the flux level is higher. Transition from anticorrelation to correlation between the pulsed fraction and the X-ray luminosity is also observed in Swift J0243.6+6124 for which the flux level of the transition is interpreted as the critical luminosity (Wilson-Hodge et al. 2018). MAXI J1409–619 is a remarkable source that shows correlation mode switching of both power-law index

[10]At very low flux levels (see Fig. 10), the high-energy cut-off power-law model could not be applied due to the deteriorating spectral quality; therefore, only the absorbed power-law model is used. As two different spectral models are introduced, the spectral parameters at lower flux values ($\lesssim 5 \times 10^{-10}$ erg s^{-1} cm^2 or 6×10^{37} erg s^{-1}) should be examined with caution.

Downloaded from https://academic.oup.com/mnras/article/496/2/1768/5854204 by MIDDLE EAST TECHNICAL UNIVERSITY LIBRARY user on 17 August 2020

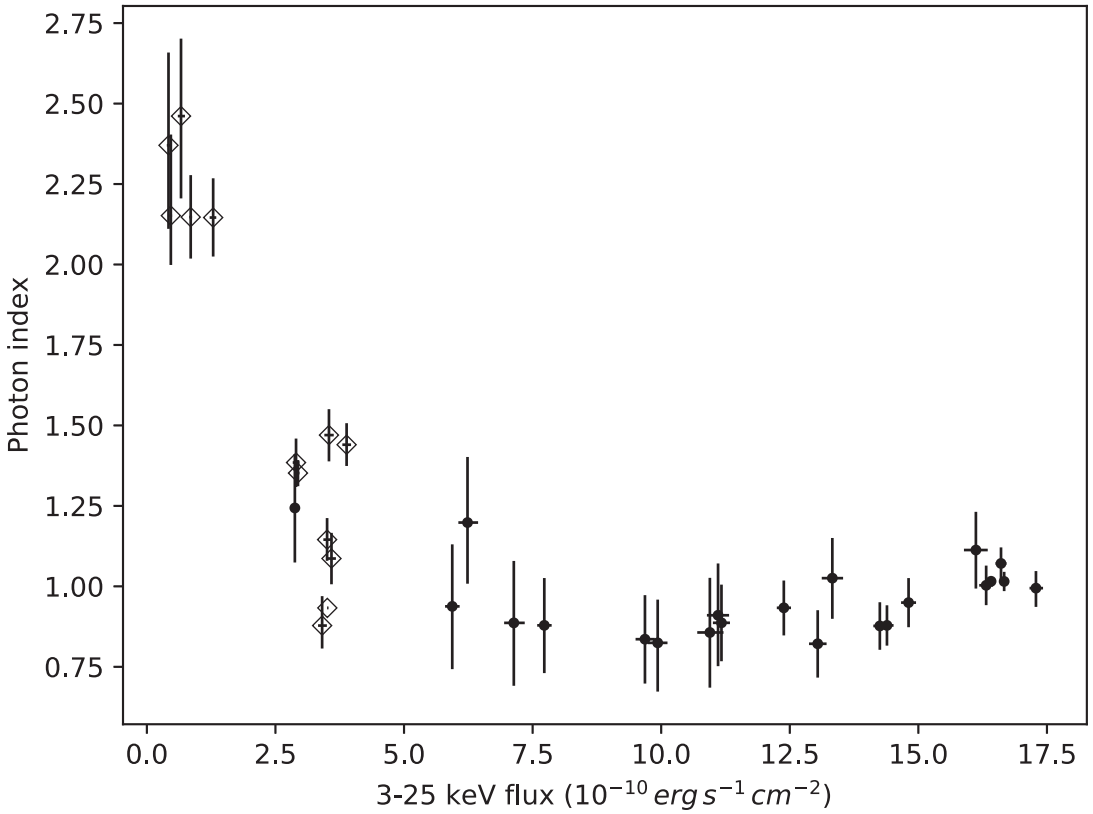


Figure 10. The relation between photon indices and fluxes of *RXTE*/PCA observations. Photon indices obtained from the spectral model without a high-energy cut-off component are plotted as diamonds. The critical luminosity of the source resides within a range of (5–10) × 10^{-10} erg s^{-1} cm^{-2} (see Section 4 for details).

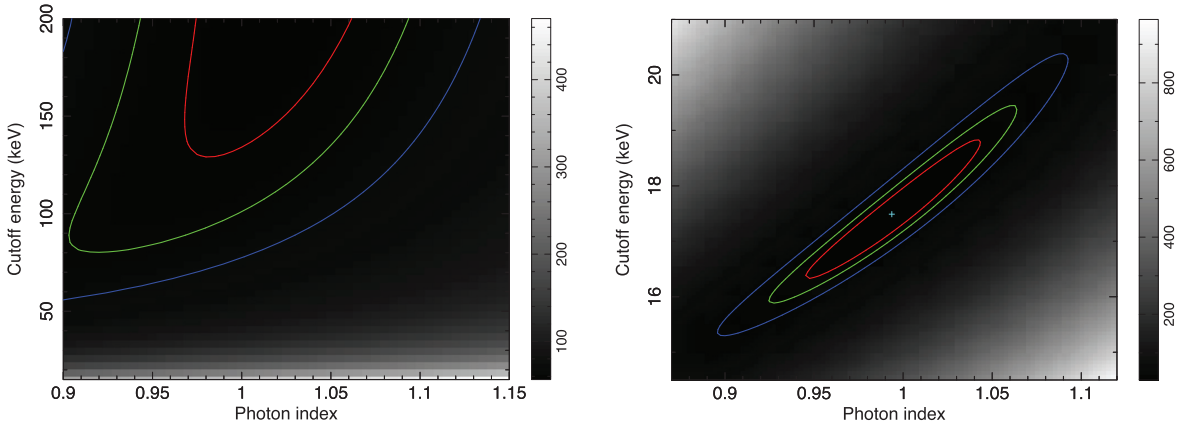


Figure 11. Confidence contour plots in the photon index–cut-off energy plane, created for *RXTE*/PCA spectral modelling. The contours correspond to the 1σ, 2σ, and 3σ confidence levels. Sidebar legends show the range of the χ^2 statistics values. Left: The cut-off energy parameter is unbounded in the spectral modelling of the observation 95358-02-01-01 (MJD 55492). Right: The cut-off energy parameter is well inside the 3–25 keV range in the spectral modelling of the observation 95441-01-01-04 (MJD 55543).

and pulse fraction around the critical luminosity. Utilizing those features, the critical luminosity level of MAXI J1409–619 can be inferred within the range of 6 × 10^{37}–1.2 × 10^{38} erg s^{-1}, where the upper limit is deduced from the starting flux level of positive photon index correlation and the lower limit is derived from the flux level beyond which the pulsed fraction anticorrelates with the count rate. Using the relation suggested by Becker et al. (2012), the inferred critical luminosity range corresponds to a magnetic field range of (3.7–7) × 10^{12} G, which might imply that the actual source luminosity is between 34 and 41 per cent of the luminosity deduced from a 15 kpc distance estimation, corresponding to a distance range between 8.7 and 9.6 kpc. Although this distance range does

Downloaded from https://academic.oup.com/mnras/article/496/2/1768/5854204 by MIDDLE EAST TECHNICAL UNIVERSITY LIBRARY user on 17 August 2020

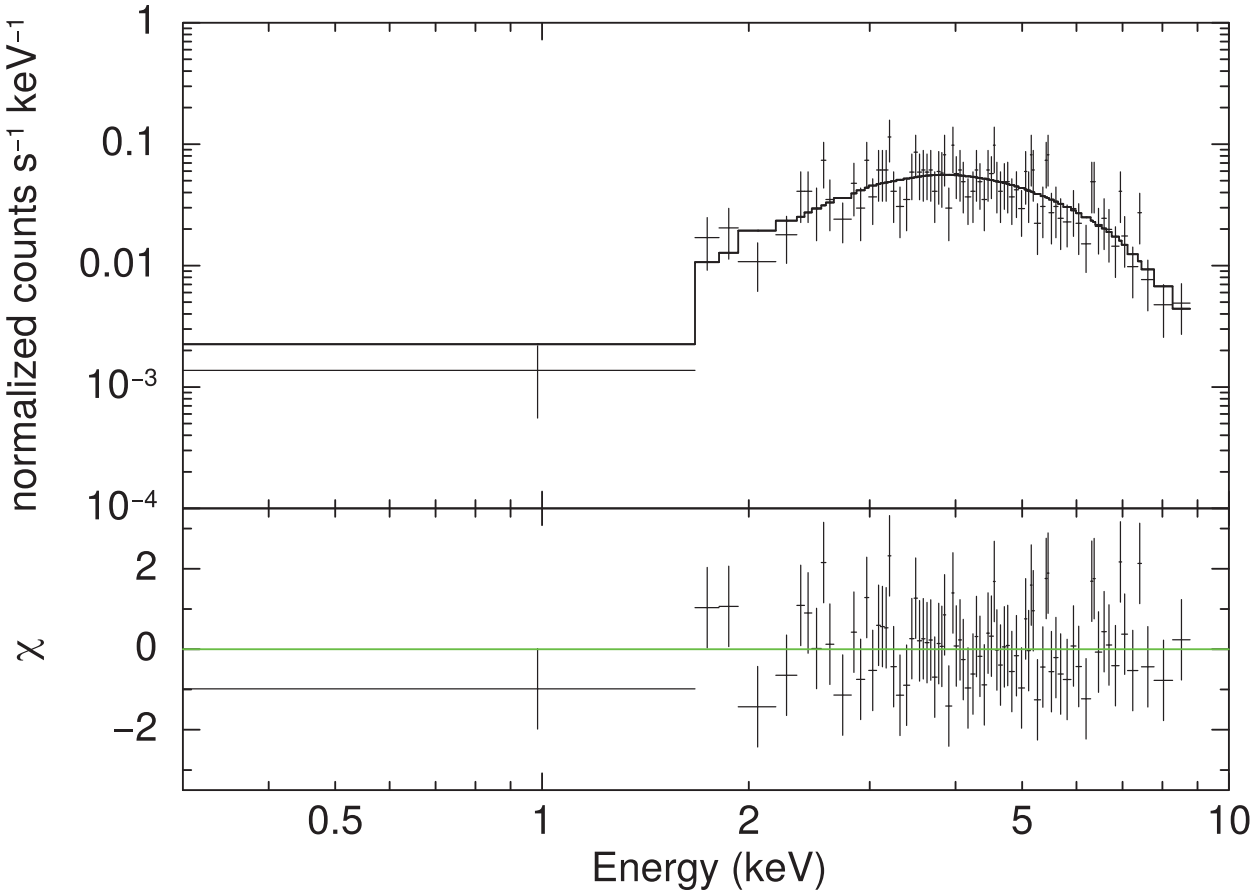


Figure 12. Upper panel: *Swift*/XRT spectrum of MAXI J1409−619 with a power-law model fit (MJD 55501–55503; Group 4 in Table 3). Lower panel: Residuals of the fit in σ values.

Table 3. Spectral parameters of *Swift*/XRT data. The flux values are calculated in the 0.5–10 keV energy band. The parameters with asterisk marks (∗) are kept fixed during spectral fitting of the given group.

	Group 1	Group 2	Group 3	Group 4	Group 5	Group 6
Obs. midtime (MJD)	55490.89	55493.19	55498.34	55502.52	55530.86	55583.68
Exposure (s)	3590	3305	2111	2051	2597	4615
$n_{\rm H}$ ($\times 10^{22}$ cm^{-2})	$5.43^{+0.74}_{-0.66}$	$3.78^{+0.98}_{-0.86}$	$2.99^{+1.11}_{-0.96}$	$5.35^{+1.65}_{-1.41}$	$5.21^{+0.63}_{-0.59}$	$9.08^{+4.44}_{-3.47}$
Photon index	0.73∗	$0.73^{+0.32}_{-0.31}$	$0.30^{+0.36}_{-0.35}$	$1.03^{+0.46}_{-0.43}$	$0.89^{+0.18}_{-0.18}$	$1.78^{+1.00}_{-0.90}$
Flux (10^{-10} erg s^{-1} cm^{-2})	$1.54^{+0.13}_{-0.12}$	$1.31^{+0.13}_{-0.11}$	$2.15^{+0.22}_{-0.20}$	$2.01^{+0.47}_{-0.26}$	$9.98^{+0.67}_{-0.55}$	$0.21^{+0.49}_{-0.08}$
Reduced χ^2	1.0615	1.1150	0.9286	0.7237	0.99558	1.163

not coincide with the most likely distance estimate reported as 15 kpc, Orlandini et al. (2012) did not rule out the possibility of a source distance of ∼7.9 kpc, which is more compatible with this range.

From the phase-resolved spectrum of the source presented in Fig. 13, we find that the neutral hydrogen column density $n_{\rm H}$ does not show a phase dependence whereas the power-law index and equivalent width of the iron line tend to have an anticorrelation with the source flux. Higher photon index values at the minimum flux can be explained by hard emission of the polar region. As the pulsed flux diminishes, the observed emission is softened. At the pulse minima, the high-energy cut-off value goes out of spectral fitting range (3–25 keV for *RXTE* observations). This is probably the result of the decreased signal-to-noise ratio due to the decreased count rate of the source. In addition, the phase bins corresponding to the pulse minima have larger χ^2 values, possibly owing to the excess high-energy cut-off values obtained by the fit and the smaller signal-to-noise ratios as explained above (see Fig. 15 for examples of low and high χ^2 spectra). A possible explanation for the increased equivalent width of the Gaussian iron Kα line at pulse minimum is the arise of 7.04 keV Kβ line emission as the emission from the hotspot fades from view. Along with the 6.4 keV Kα line emission, the blending of two iron lines results in Gaussian line broadening (Serim et al. 2017). The broadening of the iron line at lower flux might be explained by the emergence of Kβ emission when the enhanced emission of the hotspot fades

Downloaded from https://academic.oup.com/mnras/article/496/2/1768/5854204 by MIDDLE EAST TECHNICAL UNIVERSITY LIBRARY user on 17 August 2020

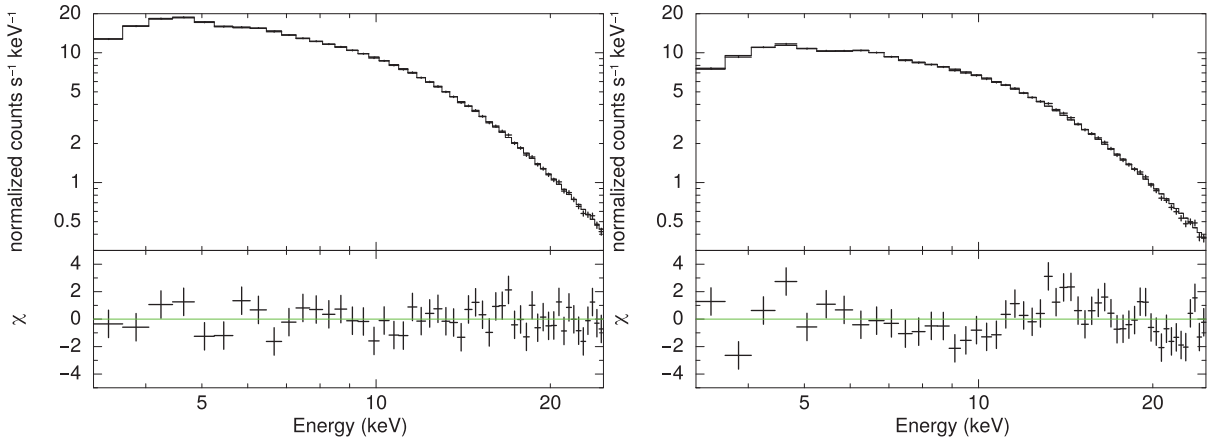


Figure 13. Two fitted phase-resolved *RXTE*/PCA spectra with residuals for comparison. Left: The spectrum of phase 0.3 with a low $\chi^2 = 0.94$. Right: The spectrum of phase 0.3 with a high $\chi^2 = 1.90$.

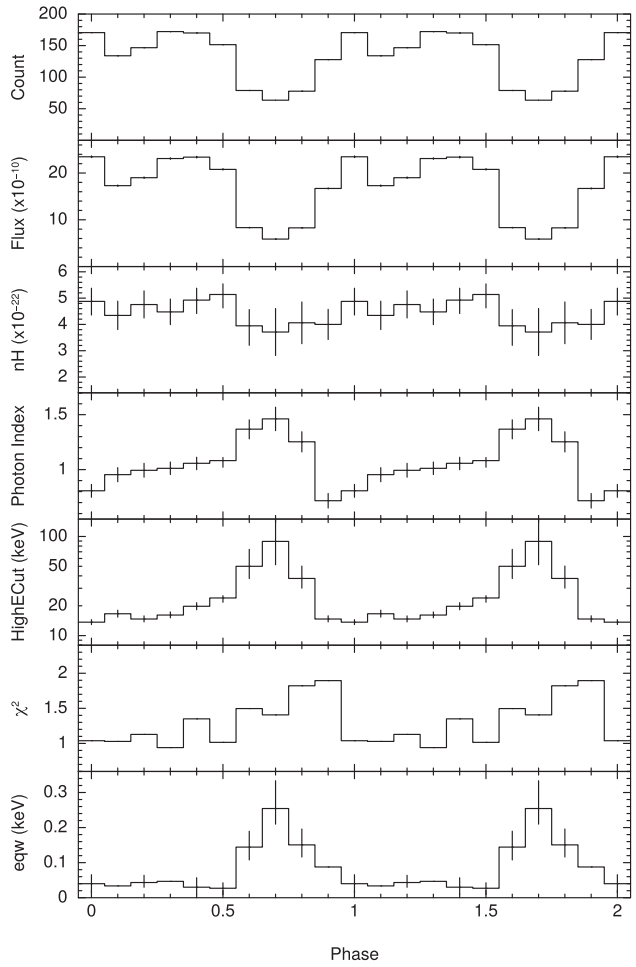


Figure 14. From top to bottom, the panels show the evolution of count rates, flux at 3–25 keV energy band, hydrogen column density, photon index, cut-off energy, reduced χ^2, and equivalent width of the Gaussian component of *RXTE*/PCA observations over phase in MJD 55541–55542. The errors in count rates and flux are too small to be seen in the figure.

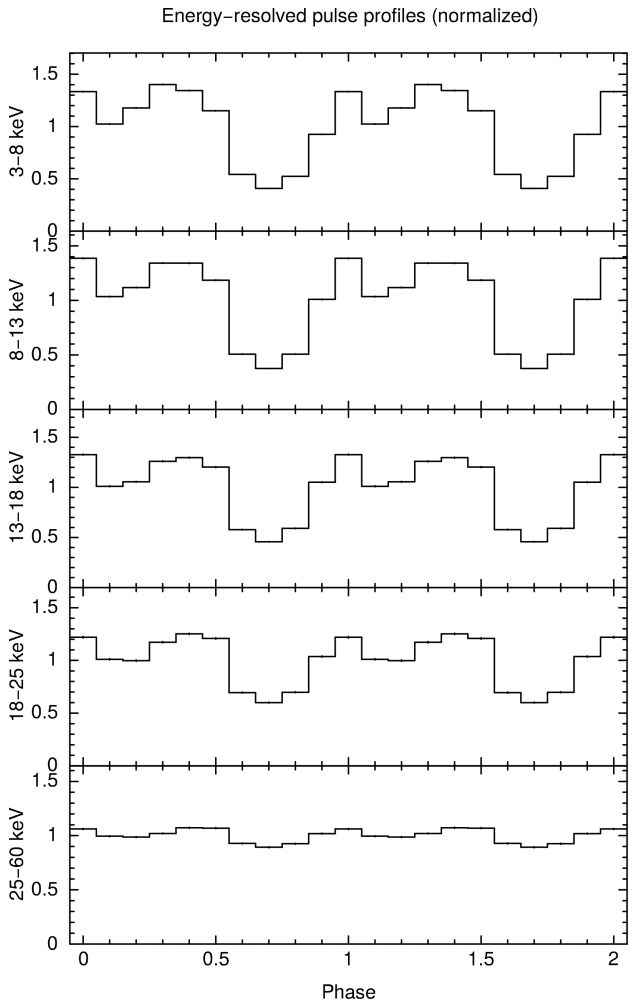


Figure 15. Normalized energy-resolved pulse profiles at various energy ranges of *RXTE*/PCA observations in MJD 55541–55542. The errors in the pulse profiles are too small to be seen.

Downloaded from https://academic.oup.com/mnras/article/496/2/1768/5854204 by MIDDLE EAST TECHNICAL UNIVERSITY LIBRARY user on 17 August 2020

away. Anticorrelation of the power-law index and flux implies that the pulsed emission is relatively hard when compared to the pulse minima.

ACKNOWLEDGEMENTS

We acknowledge support from TÜBİTAK, the Scientific and Technological Research Council of Turkey, through the research project MFAG 118F037. AB acknowledges MPE and Werner Becker for helpful discussions. We would like to express our gratitude to the anonymous referee for the valuable remarks that enabled us to improve the manuscript.

REFERENCES

Acuner Z., İnam S. Ç., Şahiner Ş., Serim M. M., Baykal A., Swank J., 2014, MNRAS, 444, 457
Anders E., Grevesse N., 1989, Geochimica Cosmochimica Acta, 53, 197
Baykal A., Oegelman H., 1993, A&A, 267, 119
Baykal A., Inam S. Ç., Stark M. J., Heffner C. M., Erkoca A. E., Swank J. H., 2007, MNRAS, 374, 1108
Becker P. A. et al., 2012, A&A, 544, A123
Bildsten L. et al., 1997, ApJS, 113, 367
Burrows D. N. et al., 2005, Space Sci. Rev., 120, 165
Camero-Arranz A., Finger M. H., Jenke P., 2010, Astron. Telegram, 3069, 1
Cash W., 1979, ApJ, 228, 939
Coburn W., Heindl W. A., Rothschild R. E., Gruber D. E., Kreykenbohm I., Wilms J., Kretschmar P., Staubert R., 2002, ApJ, 580, 394
Cordes J. M., 1980, ApJ, 237, 216
Deeter J. E., 1984, ApJ, 281, 482
Deeter J. E., Boynton P. E., 1985, in Hayakawa S., Nagase F., eds, Proc. Inuyama Workshop: Timing Studies of X-Ray Sources. Nagoya Univ., Nagoya, p. 29
Dugair M. R., Jaisawal G. K., Naik S., Jaaffrey S. N. A., 2013, MNRAS, 434, 2458
Epili P., Naik S., Jaisawal G. K., Gupta S., 2017, MNRAS, 472, 3455
Farinelli R., Ferrigno C., Bozzo E., Becker P. A., 2016, A&A, 591, A29
Finger M. H., Wilson R. B., Harmon B. A., 1996, ApJ, 459, 288
Gehrels N. et al., 2004, ApJ, 611, 1005
Ghosh P., 1994, in Holt S., Day C. S., eds, AIP Conf. Ser. Vol. 308, The Evolution of X-ray Binaries. Am. Inst. Phys., New York, p. 439
Ghosh P., Lamb F. K., 1979a, ApJ, 232, 259
Ghosh P., Lamb F. K., 1979b, ApJ, 234, 296
Gupta S., Naik S., Jaisawal G. K., 2019, MNRAS, 490, 2458
İçdem B., Baykal A., Inam S. Ç., 2012, MNRAS, 419, 3109
İnam S. Ç., Baykal A., Scott D. M., Finger M., Swank J., 2004a, MNRAS, 349, 173
İnam S. Ç., Baykal A., Swank J., Stark M. J., 2004b, ApJ, 616, 463
Jahoda K., Swank J. H., Giles A. B., Stark M. J., Strohmayer T., Zhang W. W., Morgan E. H., 1996, Proc. SPIE, 2808, 59
Jahoda K., Markwardt C. B., Radeva Y., Rots A., Stark M. J., Swank J. H., Strohmayer T. E., Zhang W., 2006, ApJS, 163, 401
Kaur R. et al., 2010, Astron. Telegram, 3082, 1
Kennea J. A., Krimm H., Romano P., Mangano V., Curran P., Evans P., 2010a, Astron. Telegram, 2962, 1
Kennea J. A., Curran P., Krimm H., Romano P., Mangano V., Evans P. A., Yamaoka K., Burrows D. N., 2010b, Astron. Telegram, 3060, 1
Klochkov D., Staubert R., Santangelo A., Rothschild R. E., Ferrigno C., 2011, A&A, 532, A126
Klus H., Ho W. C. G., Coe M. J., Corbet R. H. D., Townsend L. J., 2014, MNRAS, 437, 3863
Kluźniak W., Rappaport S., 2007, ApJ, 671, 1990
Lamb F. K., Shibazaki N., Alpar M. A., Shaham J., 1985, Nature, 317, 681
Leahy D. A., Elsner R. F., Weisskopf M. C., 1983, ApJ, 272, 256
Magdziarz P., Zdziarski A. A., 1995, MNRAS, 273, 837
Malacaria C., Klochkov D., Santangelo A., Staubert R., 2015, A&A, 581, A121
Mönkkönen J., Tsygankov S. S., Mushtukov A. A., Doroshenko V., Suleimanov V. F., Poutanen J., 2019, A&A, 626, A106
Mushtukov A. A., Suleimanov V. F., Tsygankov S. S., Poutanen J., 2015, MNRAS, 447, 1847
Orlandini M., Frontera F., Masetti N., Sguera V., Sidoli L., 2012, ApJ, 748, 86
Pringle J. E., Rees M. J., 1972, A&A, 21, 1
Roy J. et al., 2019, ApJ, 872, 33
Scott D. M., Finger M. H., Wilson C. A., 2003, MNRAS, 344, 412
Serim M. M., Şahiner S., Çerri-Serim D., İnam S. Ç., Baykal A., 2017, MNRAS, 469, 2509
Sguera V., Orlandini M., Frontera F., Bazzano A., Bird A. J., 2010, Astron. Telegram, 2965, 1
Torkelsson U., 1998, MNRAS, 298, L55
Ueno S. et al., 2010, Astron. Telegram, 3067, 1
van der Klis M., 1988, in Proc. NATO Advanced Study Institute Timing Neutron Stars, Çeşme, Turkey, 4 - 15 April 1988, NATO Advanced Study Institutes Series. Series C, Mathematical and Physical Sciences. Kluwer, Dordrecht, p. 27
van der Klis M., Stella L., White N., Jansen F., Parmar A. N., 1987, ApJ, 316, 411
Verner D. A., Ferland G. J., Korista K. T., Yakovlev D. G., 1996, ApJ, 465, 487
Wilson-Hodge C. A. et al., 2018, ApJ, 863, 9
Yamamoto T. et al., 2010, Astron. Telegram, 3070, 1
Yamaoka K. et al., 2010, Astron. Telegram, 2959, 1

This paper has been typeset from a TEX/LATEX file prepared by the author.

Downloaded from https://academic.oup.com/mnras/article/496/2/1768/5854204 by MIDDLE EAST TECHNICAL UNIVERSITY LIBRARY user on 17 August 2020